ACS OMEGA

http://pubs.acs.org/journal/acsodf

Article

Nickel Hydroxide Nanosheets Prepared by a Direct Manual Grinding Strategy for High-Efficiency Catalytic Combustion of Methane

Kun Chen, Wenzhi Li,* Ge Guo, Chen Zhu, Wenjian Wu, and Liang Yuan

Cite This: *ACS Omega* 2022, 7, 8536−8546

Read Online

ACCESS | Metrics & More | Article Recommendations | Supporting Information

ABSTRACT: Nickel hydroxide nanosheets were prepared by a very simple direct manual grinding strategy and then calcined at 200, 300, 400, and 500°. The synthesized samples were tested in lean methane (1.0% CH_4, air balanced) catalytic combustion and subjected to a series of physical and chemical characterizations. The sample calcined at 200 °C ($Ni(OH)_2$-200) presented a typical nanosheet structure and the best methane catalytic activity in all the samples, which can completely catalyze methane at 400 °C. The crystal structure changed from β-$Ni(OH)_2$ to NiO at a calcination temperature of 300 °C. The β-$Ni(OH)_2$ nanosheets began to partially agglomerate into nanoparticles at 400 °C and almost transformed into nanoparticles at 500 °C. Interestingly, the original nanosheet samples $Ni(OH)_2$-200 and NiO-300 still maintained their morphology and structure although they all went through an activity test at 500 °C in a 1.0% CH_4 atmosphere, which proves that the calcination of nanosheets in a CH_4 atmosphere tended to maintain their nanosheet morphology compared with calcination in the air. Furthermore, through the activity test, X-ray photoelectron spectroscopy results, TPx, and in situ DRIFTS characterization, it was proved that the hydroxyl groups on the $Ni(OH)_2$-200 and NiO nanosheets were beneficial to the dissociation of methane on the catalyst surface, and the nanosheet structure was also prone to generating more active adsorbed oxygen, so the activation energy of methane was lowered. A methane catalytic mechanism on the $Ni(OH)_2$ nanosheets and NiO nanoparticles was proposed, which further proved the key role of hydroxyl groups in methane combustion.

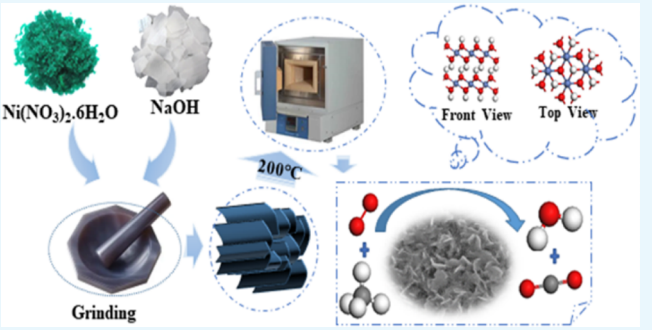

1. INTRODUCTION

Methane has been increasingly exploited as a substitute for conventional fossil fuels due to its abundant reserves and high economic benefits since the shale revolution.[1−5] The engines of vehicles using natural gas or liquefied petroleum gas usually perform combustions of methane at a relatively low temperature (<600 °C), and the greenhouse effect caused by the released unburned methane is on average 28 times more powerful than CO_2.[6,7] As countries around the world promulgate more stringent emission legislation, it is urgent to find a method capable of lean methane combustion with high efficiency and low cost.[1,8−16] The catalytic combustion of methane is considered to be a methane treatment method with great potential, which can efficiently convert methane into harmless water and CO_2 at a lower temperature in the presence of a suitable catalyst, while suppressing the production of harmful air pollutants (such as NO_x, CO, and SO_x).[3,10,17−28]

Noble metal (Pd, Pt, Ru, Rh, Au, etc.)-supported catalysts are generally used for CH_4 elimination and Pd-supported catalysts have been reported to be highly active[12,16−18,22,29−34] mainly because of their ability to break the C−H bond with high binding energy in CH_4 under a relatively low energy barrier.[5,18,22,32,35−38] Although noble metal-supported catalysts have high efficiency, their high price, limited source, sintering issue, and poisoning tendency limit their large-scale application.[3,10,15,39,40] Accordingly, the development of alternative catalysts based on non-noble metals is attractive, and single metal oxide-based catalysts such as MnO_x, Co_3O_4, CuO, Fe_2O_3, NiO, and perovskite have been found to be highly active for methane combustion.[13,21,24,41−49] NiO, a p-type semiconductor, is of particular interest because of its unique chemical properties, high thermal stability, and low prices.[50−59] Recently, NiO nanomaterials with different morphologies, such as nanosheets,[50,55,57,60−62] nanoparticles,[56,63−65] nanorods,[54,66] and honeycomb-like[67] nanostructures, have been reported successively and applied as catalysts, battery electrodes, and capacitors.[68] However, there are not many reports about the application of NiO catalysts in methane catalytic combustion. Ye et al. synthesized polymorphous NiO nanomaterials by a one-pot thermal decomposition approach.[69] They pointed out

Received: November 10, 2021
Accepted: February 22, 2022
Published: March 4, 2022

Scheme 1. Schematic Illustration of the Sample Synthesis Process[a]

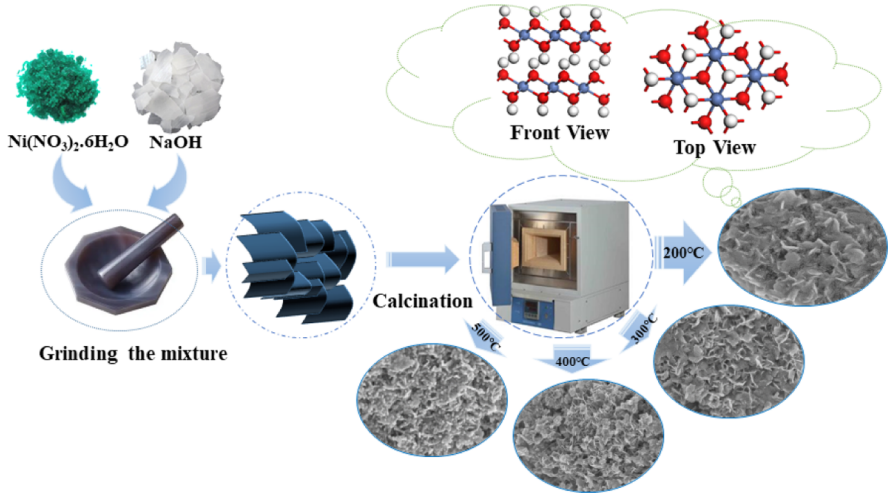

[a]White: hydrogen atom, red: oxygen atom, and blue: nickel atom.

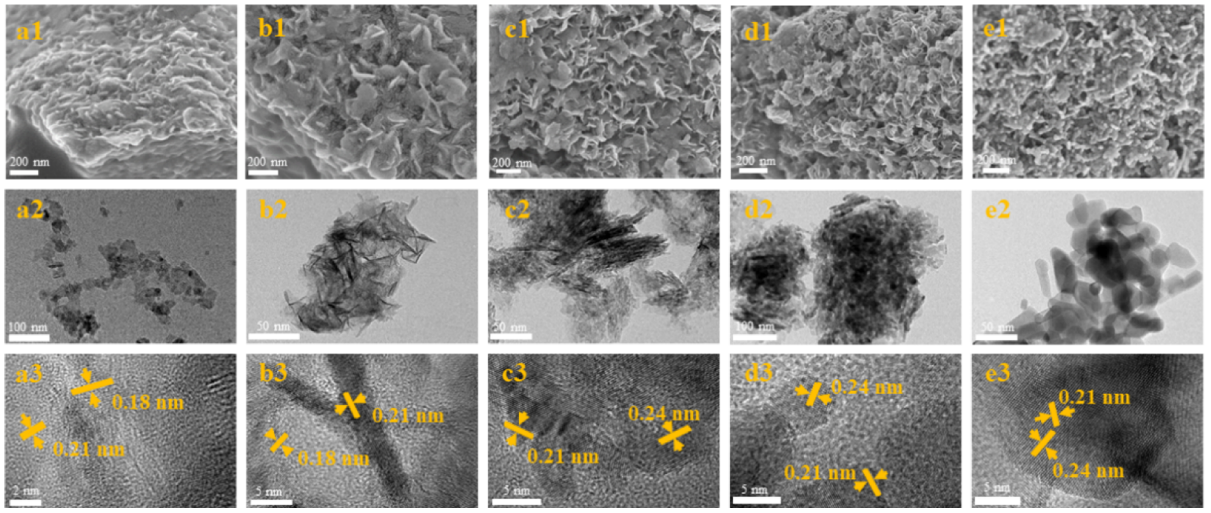

Figure 1. SEM, TEM, and HRTEM characterization of all the samples: (a1−a3) $Ni(OH)_2$, (b1−b3) $Ni(OH)_2$-200, (c1−c3) NiO-300, (d1−d3) NiO-400, and (e1−e3) NiO-500.

that NiO nanoparticle-based sheets showed the highest methane combustion activity and converted all lean methane at 450 °C owing to their small crystal size and large specific surface areas. Yu et al. prepared NiO nanosheets by the traditional NaOH liquid phase precipitation method, and the NiO nanosheets completely oxidized methane at 500 °C.[70] They found that the formation of Ni^{3+} cations was harmful to the catalytic activity. NiO nanoparticles prepared with ethylene glycol as a soft template were also applied in methane combustion and catalyzed methane at 440 °C.[71] The abovementioned studies proved the positive performance of NiO in methane catalytic combustion, but there are still several problems remaining: (i) harmful organic reagents were used in the preparation of NiO, and the preparation process was relatively complicated. How to develop a more environmentally friendly preparation method is still a challenge; (ii) the mechanism of the methane catalytic combustion on the NiO surface has scarcely been proposed; and (iii) the changes in the morphology of NiO during the calcination and the catalysis process were rarely mentioned.

Regarding the abovementioned problems, we propose a very simple mechanical grinding method to prepare NiO nanosheets. The sodium hydroxide and nickel nitrate hexahydrate crystals were, respectively, ground uniformly and then mixed to obtain β-$Ni(OH)_2$ sheets. The β-$Ni(OH)_2$ was calcined at a suitable temperature to obtain NiO nanosheets. Compared with other preparation methods, only two chemical reagents were used in the mechanical grinding method, and the production of waste water was avoided, so the preparation was more environmentally friendly and cost-effective. The changes in the morphology of β-$Ni(OH)_2$ and NiO during the calcination and the catalysis process were characterized in detail by X-ray diffraction (XRD), Brunauer−Emmett−Teller (BET), scanning electron microscopy (SEM), high-resolution transmission electron microscopy (HRTEM), X-ray photoelectron spectroscopy (XPS), and TPx techniques. Furthermore, we proposed the reaction mechanism of the methane catalytic combustion on the NiO nanosheet surface through in situ DRIFTS.

https://doi.org/10.1021/acsomega.1c06348
ACS Omega 2022, 7, 8536−8546

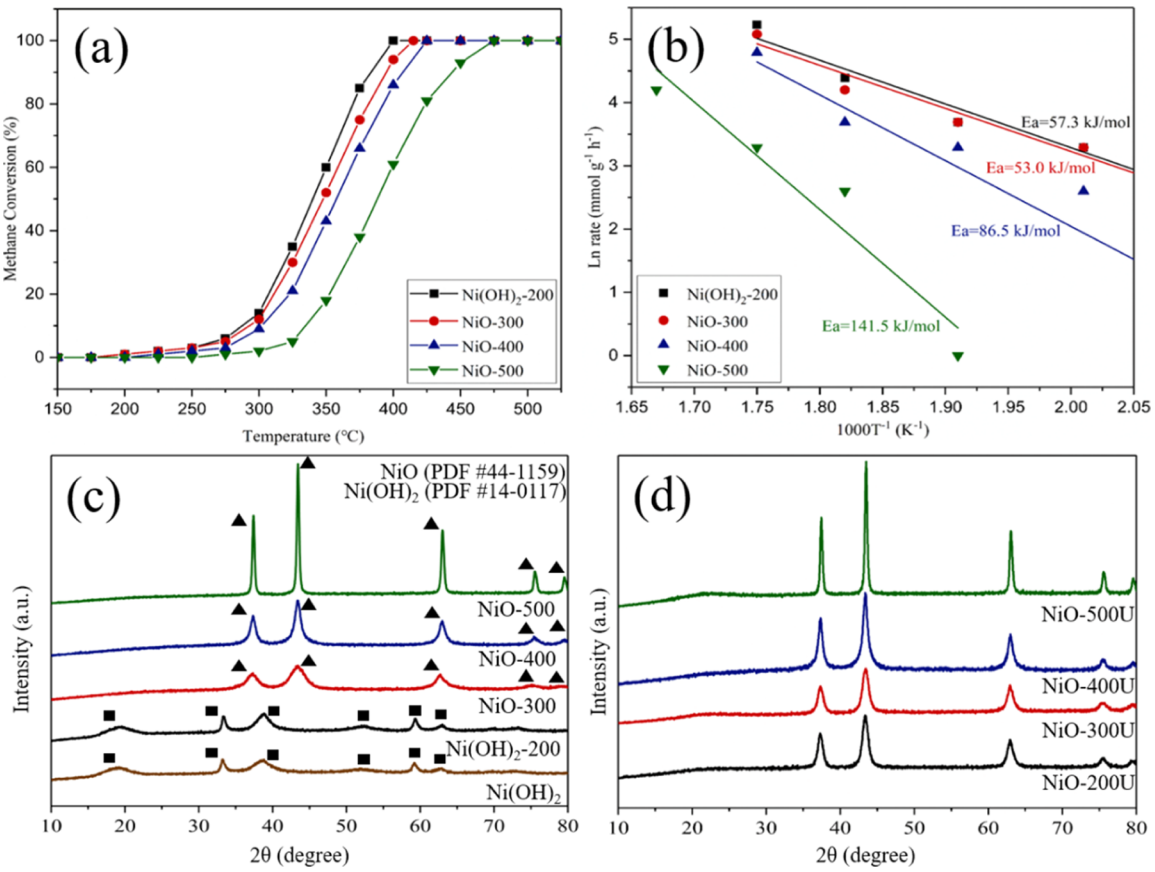

Figure 2. (a) Lean methane (1.0% CH_4 in air, 30 000 mL h^{-1} g^{-1} gas weight hourly space velocity) combustion activity on the samples prepared. (b) Apparent activation energies (E_a) calculated from the Arrhenius formula. The XRD patterns of the (c) fresh samples and the (d) used samples.

2. EXPERIMENTAL SECTION

2.1. Catalyst Synthesis. β-$Ni(OH)_2$, the precursor of $Ni(OH)_2$ and NiO nanosheets, was prepared by a simple direct manual grinding. Typically, 10 mmol $Ni(NO_3)_2{\cdot}6H_2O$ and 20 mmol NaOH were mechanically ground in an agate mortar to achieve uniformity, then they were mixed together and ground for another 30 min until a green paste-like β-$Ni(OH)_2$ was formed. Afterward, the product was washed with deionized water and centrifuged three times. The β-$Ni(OH)_2$ was finally dried in an oven at 60 °C for 24 h and is labeled as $Ni(OH)_2$ in the discussion that follows.

The as-synthesized precursor β-$Ni(OH)_2$ was calcined in air at 200, 300, 400, and 500 °C for 2 h, respectively, using a ramp of 5 °C min^{-1} to obtain the final catalysts. According to the difference of the calcination temperature and the crystal phase, these catalysts are labeled as $Ni(OH)_2$-200, NiO-300, NiO-400, NiO-500, respectively. The schematic illustration of the synthesis process is presented in Scheme 1, including the front view and top view of sample $Ni(OH)_2$-200. From the front view of sample $Ni(OH)_2$-200, it can be seen that it presented a typical layered structure.

2.2. Characterization of Catalysts. Characterizations such as XRD, SEM, TEM, TPx, BET, XPS, and in situ DRIFTS were used to characterize the physical and chemical properties of the samples. The detailed experimental parameters are shown in the Supporting Information.

2.3. Measurement of Methane Combustion Activity. 20 mg of each sample was used as the reaction catalyst, and the inlet gas (1.0% CH_4, air balanced) was maintained at 10 mL min^{-1} (10 sccm) using a mass flow controller. The gas weight hourly space velocity was 30,000 mL h^{-1} g^{-1}. The detailed parameters are shown in the Supporting Information.

3. RESULTS AND DISCUSSION

3.1. Morphological Structures of the Samples. The SEM, TEM, and HRTEM characterization of all the samples is shown in Figure 1. It can be seen from Figure 1(a1) that the precursor prepared by the mechanical grinding method presents a relatively regular nanosheet structure. After calcination at 200 °C, $Ni(OH)_2$-200 still exhibited a nanosheet structure, but the arrangement became more disordered. The lattice spacing on the surface of these two samples was 0.18 and 0.21 nm, corresponding to the (1 0 0) and (1 0 1) crystal planes of β-$Ni(OH)_2$ (JCPDS PDF # 14-0117),[72] respectively. As the calcination temperature increased to 300 °C, NiO-300 still presented a disordered nanosheet structure, but it can be seen from Figure 1(c2) that some nanosheets began to aggregate. The lattice spacing was 0.21 and 0.24 nm, corresponding to the (1 1 1) and (2 0 0) crystal planes of NiO (JCPDS PDF # 44-1159),[73] respectively, indicating that the sample converted to NiO under the calcination at 300 °C. When the calcination temperature was further increased, NiO-400 gathered and partially converted into nanoparticles, while NiO-500 was basically NiO nanoparticles.

The stability test results of $Ni(OH)_2$-200 at 400 °C for 50 h are shown in Figure S1, which shows that the catalyst presented good stability. The SEM images of the used samples are shown in Figure S2. Interestingly, the original nanosheet samples $Ni(OH)_2$-200 and NiO-300 still maintained their

https://doi.org/10.1021/acsomega.1c06348
ACS Omega 2022, 7, 8536−8546

Table 1. XRD Analysis Data, Physical Properties, and Activity Results of Catalysts

samples	2θ (deg)	(hkl)	D^a/nm	S_{BET} (m^2/g)	$V_{pores}{}^b$(cm^3/g)	T_{100} (°C)
$Ni(OH)_x$	19.3, 33.1, 38.5	(001), (100), (101)	2.50, 12.90, 4.20			
$Ni(OH)_x$-200	19.3, 33.1, 38.5	(001), (100), (101)	2.90, 14.20, 6.10	156.0	0.24	400 °C
NiO-300	37.2, 43.3, 62.9	(101), (012), (110)	7.10, 7.60, 12.60	157.7	0.26	415 °C
NiO-400	37.2, 43.3, 62.9	(101), (012), (110)	9.90, 9.20, 10.10	93.4	0.18	425 °C
NiO-500	37.2, 43.3, 62.9	(101), (012), (110)	25.40, 26.30, 27.00	13.8	0.10	475 °C

[a]Crystallite sizes of the samples calculated by the Scherrer equation ($D = K\lambda/(\beta \cos \theta)$). [b]Volume of pores calculated by the Barrett–Joyner–Halenda method.

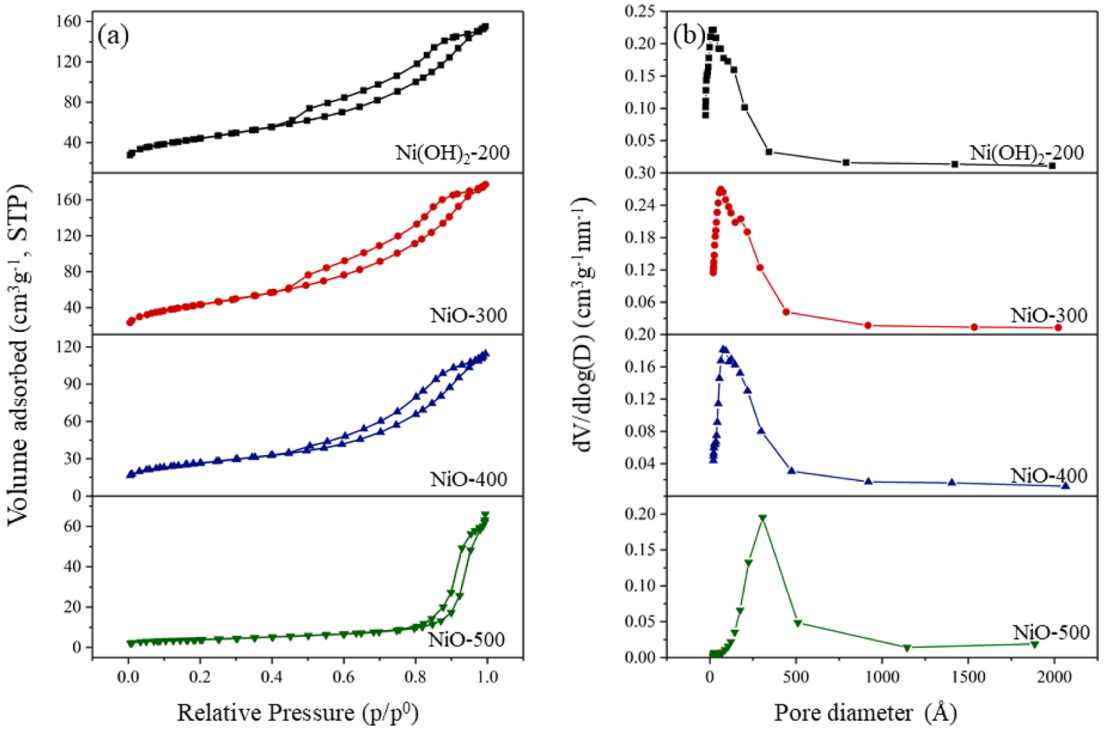

Figure 3. (a) N_2 adsorption–desorption isotherms and the (b) corresponding pore size distribution of the samples.

morphology and structure although they all went through the calcination process at 500 °C in a 1.0% CH_4 atmosphere. The samples NiO-400 and NiO-500, composed of nanosheets and nanoparticles, were more inclined to agglomerate and completely transform into nanoparticles. These results prove that the calcination of NiO nanosheets in a CH_4 atmosphere tended to maintain their nanosheet morphology compared with calcination in the air.

3.2. Activity Determination and Physical Characterizations. The catalyst activity test results are shown in Figure 2. Figure 2a shows the curve of methane conversion with temperature on the four samples. Figure 2b shows the apparent activation energies (E_a) which were calculated from the Arrhenius formula: $k = A \cdot \exp(-E_a/RT)$ in the category of reaction kinetics.[74,75] The complete methane conversion temperatures of the four samples $Ni(OH)_2$-200, NiO-300, NiO-400, and NiO-500 were 400, 415, 425, and 475 °C, respectively. With the increase in the calcination temperature, the activity of the catalyst gradually decreased, and when the calcination temperature reached 500 °C, the activity decreased more obviously. When one considers the SEM and HRTEM characterization results, it is not difficult to find that the morphology had an important effect on the catalytic activity, and the activity of nanosheets was significantly higher than that of NiO nanoparticles. When the nanosheets were completely converted into nanoparticles, the catalytic activity was significantly reduced. The sample $Ni(OH)_2$-200 was highly active in non-noble metal methane combustion (activity results from other research are shown in Table S1). It can also be clearly seen from Figure 2b that the activation energies of samples $Ni(OH)_2$-200 (57.3 kJ/mol) and NiO-300 (53.0 kJ/mol) with the nanosheet morphology were almost the same. The apparent activation energy of NiO-400 (86.5 kJ/mol) increased to a certain extent, and when the nanosheets were completely converted into nanoparticles, the apparent activation energy of NiO-500 (141.5 kJ/mol) was the highest. The results indicate that there was a close correlation between the methane catalytic combustion activity and the morphology of the catalysts, and the catalytic activity of the $Ni(OH)_2$ and NiO nanosheets was higher than that of the NiO nanoparticles.

The XRD patterns of the fresh and used samples are shown in Figure 2c. The crystallite sizes perpendicular to the specific crystal planes are shown in Table 1. The results show that the $Ni(OH)_2$ prepared after mechanical grinding presented the crystal structure of β-$Ni(OH)_2$ (JCPDS PDF # 14-0117), and the calcination at 200 °C made no obvious effect on the crystal structure of the sample. The prominent diffraction peaks located at 19.3°, 33.1°, and 38.5° corresponded to the (0 0 1), (1 0 0), and (1 0 1) planes, respectively. For these two samples, it can be seen from Table 1 that the crystallite sizes

https://doi.org/10.1021/acsomega.1c06348
ACS Omega 2022, 7, 8536–8546

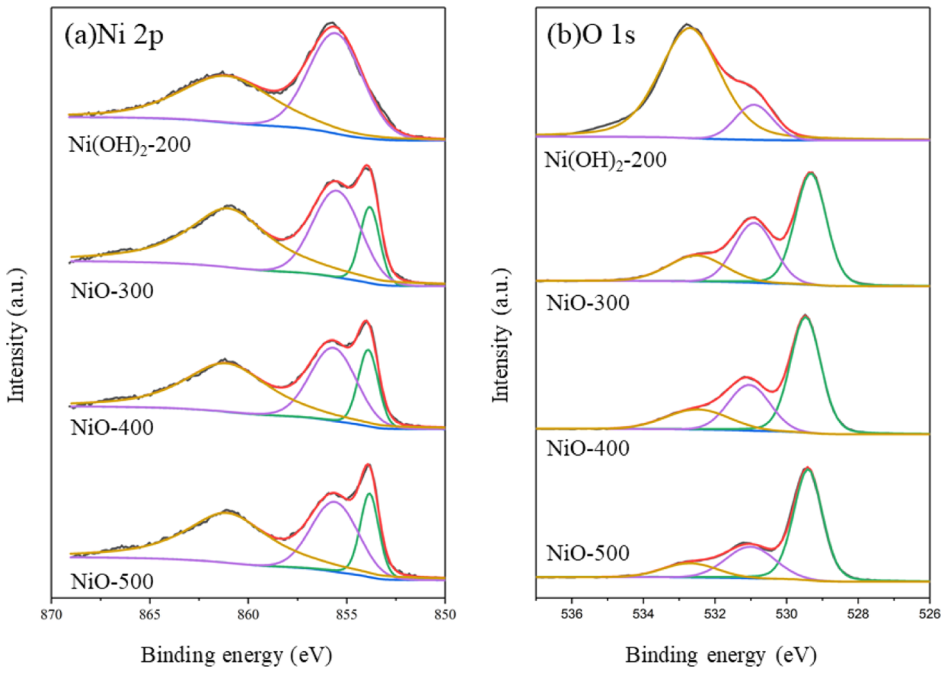

Figure 4. XPS results of (a) Ni 2p and (b) O 1s spectra of all the samples.

perpendicular to the (0 0 1) crystal plane were 2.50 and 2.90 nm, which were significantly lower than those perpendicular to the other two crystal planes. This explains, to a certain extent, its unique sheet structure. As the calcination temperature further increased to 300 °C and above, the samples all showed the typical crystal structure of NiO (JCPDS PDF # 44-1159), which proved that β-Ni(OH)$_2$ was converted into NiO between the calcination temperature of 200−300 °C. The prominent peaks located at 37.2°, 43.3°, and 62.9° corresponded to the (1 0 1), (0 1 2), and (1 1 0) crystal planes, respectively. The crystallinity of the samples gradually increased and the crystallite sizes perpendicular to the three prominent crystal planes tended to be larger and uniform (25.40, 26.30, and 27.00 nm for NiO-500), indicating that the NiO nanosheets transformed into NiO nanoparticles with the increasing temperature. The results are consistent with the abovementioned SEM and TEM characterizations.

The XRD spectra of the used samples are shown in Figure 2d. It is interesting to note that the crystallinity of the used samples was significantly different, although all the samples were calcined at 500 °C in a 1.0% CH_4 atmosphere. The crystallinity of NiO-200U and NiO-300U was obviously lower than that of NiO-500U. Combined with the SEM and TEM characterization, the results indicate that if the NiO nanosheets were directly calcined at 500 °C in the air, they would be transformed into more stable NiO nanoparticles with lower surface energy; if the Ni(OH)$_2$-200 nanosheets were calcined in a 1.0% CH_4 atmosphere at 500 °C, they tended to maintain the original morphology due to the continuous CH_4 adsorption and CO_2 desorption on the surface of the nanosheets. The results explain why the crystallinity of NiO-200U and NiO-300U is lower than that of NiO-500U. As for NiO-400, calcination at 500 °C in a 1.0% CH_4 atmosphere improved its crystallinity because of its inherently mixed nanoparticles and nanosheets. The particle size distributions of the samples NiO-500 and NiO-500U are shown in Figure S3. The average particle size of the catalyst NiO-500 increased significantly after the stability test, from 42.1 to 72.5 nm, and the particle size distribution became more uneven.

Figure 3 shows the N_2 adsorption−desorption isotherms and the corresponding pore size distribution of the samples. The curves of Ni(OH)$_2$-200, NiO-300, and NiO-400 were type IV isotherms with an H3 hysteresis loop, and the three samples presented the mesoporous structure.[76,77] It indicates that there were slit-like holes formed by the cross-linking of nanosheets in the samples. The Ni(OH)$_2$-200 and NiO-300 samples with a nanosheet structure had almost the same specific surface area and pore volume (shown in Table 1), and both were higher than the NiO-400 sample with the hybrid of nanoparticles and nanosheets. Differently, the curve of NiO-500 was closer to a type IV isotherm with an H4 hysteresis loop. In combination with the pore size distribution, it can be seen that the H4 hysteresis loop represented the existence of macropores in the sample.[78] These macropores were considered to be gaps between NiO nanoparticles because there was basically no nanosheet structure but nanoparticles in the sample NiO-500. The specific surface area and pore volume of NiO-500 (shown in Table 1) were the lowest among the four samples, thereby reducing its methane catalytic activity.

3.3. Chemical Properties and Possible Reaction Mechanism. The XPS results are shown in Figure 4, which characterizes the chemical valence states of Ni and O on the surface. It can be seen from the Ni 2p spectra (Figure 4a) that there were two valence states of Ni on the surface of the sample, namely Ni^{2+} and Ni^{3+}.[71] For samples NiO-300, NiO-400, and NiO-500 with a NiO crystal form, the presence of Ni^{3+} did not mean the presence of the Ni_2O_3 crystal phase. NiO is a p-type semiconductor and will form Ni^{2+} defects, therefore two contiguous Ni^{2+} will lose an extra electron to form Ni^{3+} in order to maintain a charge balance. A split peak in the interval 852.0−858.0 eV was not shown in the Ni 2p spectra of Ni(OH)$_2$-200, which differed from the other three samples and further demonstrated its Ni(OH)$_2$ structure. Our previous work pointed out that Ni^{2+} might be responsible for

https://doi.org/10.1021/acsomega.1c06348
ACS Omega 2022, 7, 8536−8546

Table 2. XPS Result Analysis of the Samples

	O 1s									
	O_{latt}		O_{ads}		O_{OH}		Ni 2p			
samples	BE (eV)	at.	BE (eV)	at.	BE (eV)	at.	$(O_{ads} + O_{OH})/O_{sum}$ [a]	Ni^{2+}	Ni^{3+}	Ni^{2+}/Ni^{3+}
$Ni(OH)_2$-200			530.9	0.14	532.7	0.86	1.00	861.1	855.6	0.97
NiO-300	529.3	0.49	530.9	0.31	532.5	0.20	0.51	861.0, 853.8	855.5	2.03
NiO-400	529.4	0.55	531.0	0.27	532.5	0.18	0.45	861.1, 853.9	855.7	2.07
NiO-500	529.4	0.61	531.0	0.26	532.7	0.13	0.39	861.0, 853.8	855.6	2.10

[a] O_{sum} refers to the accumulation of O_{latt}, O_{ads}, and O_{OH} areas.

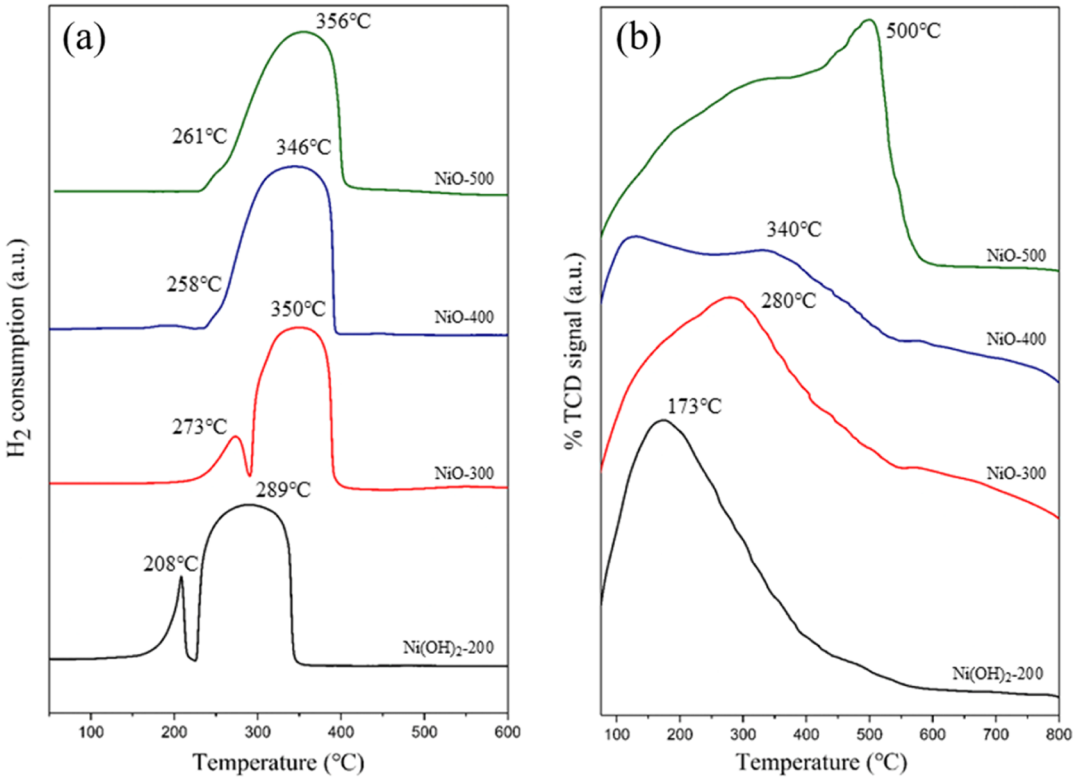

Figure 5. (a) H_2-TPR and (b) O_2-TPD results of all the samples.

the enhanced methane activity instead of Ni^{3+},[72] so we calculated the content of Ni^{2+} and Ni^{3+} in each sample, and the proportions are recorded in Table 2. The Ni^{2+}/Ni^{3+} ratios of samples NiO-300, NiO-400, and NiO-500 were very close, so the different valence states of Ni should not be the cause of the difference in the methane catalytic activity.

The O 1s spectra of all the samples are shown in Figure 4b, and each line can be deconvoluted into three peaks at ~529.4, ~531.0, and ~532.6 eV, corresponding to surface lattice oxygen (O_{latt}), adsorbed oxygen (O_{ads}), and surface hydroxyl groups (O_{OH}), respectively.[79] The quantitative results of the O content and the ratio are listed in Table 2. The surface O species of sample $Ni(OH)_2$-200 were mainly composed of hydroxyl groups (0.86), and there was also a small amount of adsorbed oxygen on the surface (0.14), which demonstrated its $Ni(OH)_2$ structure. Generally speaking, the adsorbed oxygen and hydroxyl groups on the surface of catalysts are positively correlated with the catalytic activity in methane combustion. Therefore, the sum of the two active oxygen is also counted in Table 2, where the values of NiO-300, NiO-400, and NiO-500 are 0.51, 0.45, and 0.39, respectively. This result corresponded to their catalytic performance. The lower the content of hydroxyl groups and adsorbed oxygen, the worse the corresponding catalytic activity. Furthermore, as the calcination temperature increased, the adsorbed oxygen and hydroxyl group content on the catalyst surface gradually decreased. When the calcination temperature reached 400 °C, the hydroxyl group content only decreased by 0.02, but when the calcination temperature reached 500 °C, the content decreased by 0.05. Based on the morphology of the samples, the results indicate that the hydroxyl group content of the sample was related to the morphology. More hydroxyl groups were easily exposed on the surface of the $Ni(OH)_2$ and NiO nanosheets. As the calcination temperature increased, the nanosheets gradually transformed into nanoparticles, and the hydroxyl group content on the surface decreased more obviously, reducing their methane catalytic activity.

To explore the redox properties of the samples, H_2-TPR and O_2-TPD characterizations were used, and the results are shown in Figure 5. It can be seen from Figure 5a that the reduction peak of $Ni(OH)_2$-200 is located at an obviously lower temperature than other samples. The peak at 208 °C might be attributed to the reduction of active oxygen species adsorbed on the surface, while the broad peak at 289 °C

https://doi.org/10.1021/acsomega.1c06348
ACS Omega 2022, 7, 8536−8546

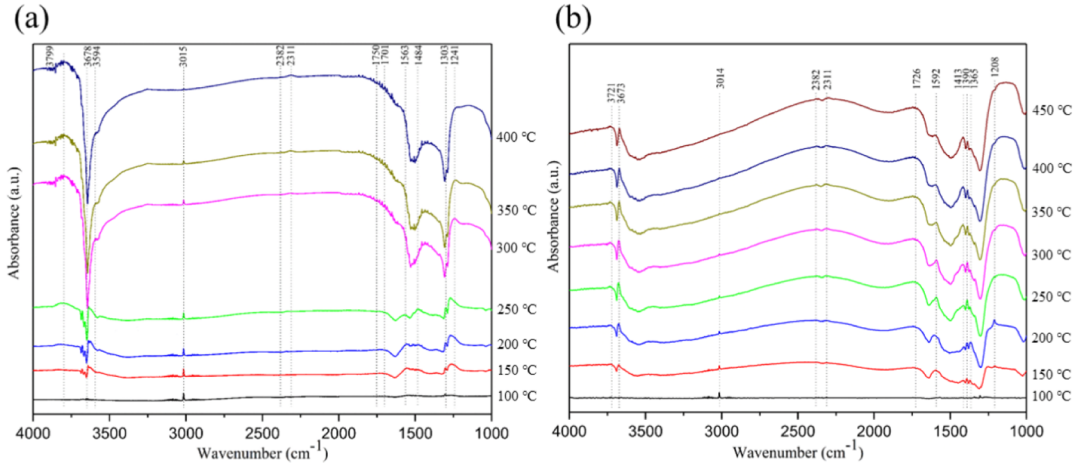

Figure 6. In situ DRIFT spectra for catalytic methane oxidation reactions using (a) $Ni(OH)_2$-200 and (b) NiO-500.

corresponded to the reduction peaks of Ni^{3+} and Ni^{2+} in the sample. For the other three samples, each curve could be deconvoluted into two peaks, located at about 260 °C and 350 °C, which were attributed to two steps: the reduction of Ni^{3+} to Ni^{2+} and the further reduction of Ni^{2+} to metallic Ni^0.[70,72] The results show that the nickel hydroxide nanosheets presented stronger redox properties than the other samples, and there were more absorbed active oxygen sites on the surface, which is consistent with the XPS results.

The O_2-TPD results are shown in Figure 1b, and the main oxygen desorption peaks are marked. As the calcination temperature increased, the main oxygen desorption peak gradually moved to the right. It can be speculated that the properties of adsorbed oxygen corresponding to these peaks were different. For $Ni(OH)_2$-200, the oxygen desorption peak located at 173 °C indicated that the oxygen was mainly in the form of surface-adsorbed oxygen.[80] The oxygen desorption peaks at 280, 340, and 500 °C corresponded to the desorption of lattice oxygen.[6] These results indicate that the double-layered structure of $Ni(OH)_2$-200 exposed more adsorbed active oxygen sites, which was conducive to methane catalytic combustion.

In order to reveal the reaction mechanism of methane catalytic combustion, the in situ DRIFT spectra of methane catalytic combustion on $Ni(OH)_2$-200 and NiO-500 are obtained and shown in Figure 6 because $Ni(OH)_2$-200 presented a representative nanosheet structure and NiO-500 presented a nanoparticle structure. The positions of some characteristic bands are shown in Table S2 and some bands in Figure 6a,b are located at almost the same positions. The band at 3015 cm^{-1} is a typical vibration of gaseous methane, and the doublet bands at 2382 cm^{-1} and 2311 cm^{-1} are typical peaks of carbon dioxide.[6] The intensity of the band at 3015 cm^{-1} decreased gradually as the temperature rose, while the bands assigned to CO_2 became significant, indicating that methane has almost converted to CO_2 on the two samples. For sample $Ni(OH)_2$-200, the band at 3015 cm^{-1} disappeared completely at 400 °C (Figure 6a), and the band for sample NiO-500 basically disappeared at 450 °C (Figure 6b). The results maintain a high consistency with the activity test results.

The in situ DRIFT results were further studied, and some differences were found between the two samples. For sample $Ni(OH)_2$-200, when the temperature reached 300 °C, there was an obvious inverted band at 3678 cm^{-1}, which indicates that the hydroxyl groups in the sample were beginning to be consumed, and the catalyst was changed from $Ni(OH)_2$ to NiO in the methane atmosphere. In the temperature range of 100−250 °C, the bands at 1563 and 1484 cm^{-1} gradually increased in intensity. The band at 1563 cm^{-1} can be considered as $\nu_{as}(COO^-)$, while the band at 1484 cm^{-1} corresponded to the δ_{as} (CH_3) in methyl groups. It indicates that in this temperature range, methane can be adsorbed on the surface of $Ni(OH)_2$-200 through the interaction between methane and Ni−OH groups and be initially activated to achieve the rupture of the first C−H bond, which means that $Ni(OH)_2$ was also efficient in the adsorption and activation of methane. In addition, the band at 1241 cm^{-1} corresponding to the vibration of the C−O bond in alcohols and the band at 1701 cm^{-1} assigned to C═O bonds in aldehydes began to appear and the intensity gradually increased in the temperature range of 100−250 °C, afterward gradually weakened and disappeared when the temperature further rose, indicating that aldehydes and alcohols may be intermediate products. As the temperature rose above 250 °C, the band at 3799 cm^{-1} became significant. We speculate that it may be caused by the free hydroxyl groups during the decomposition of $Ni(OH)_2$ into NiO. The band at 1750 cm^{-1} corresponded to the vibration of the C═O bonds in formic acid. The intensity of the band gradually increased at a temperature higher than 250 °C, indicating that formic acid was also an intermediate product and may eventually be completely converted to carbon dioxide. The DRIFT results prove that the presence of Ni−OH in $Ni(OH)_2$-200 was beneficial to the dissociation of the first C−H bond in methane, and the process is well accepted to be the rate-determining step in the catalytic combustion of methane. Therefore, the presence of hydroxyl groups was also one of the reasons why $Ni(OH)_2$-200 presented the best catalytic activity among the four samples. As the reaction temperature increased, $Ni(OH)_2$-200 was gradually decomposed into NiO, and lattice oxygen and adsorbed oxygen were also supplemented, promoting the further oxidation of oxygen-containing intermediates.

In the in situ DRIFT spectrum of sample NiO-500, the bands at 1413 and 1365 cm^{-1} corresponded to the δ_{as} (CH_3) and δ_s (CH_3) of the methyl groups, respectively. When the temperature was increased from 250 to 300 °C, the intensities of these two bands increased significantly, indicating that a higher temperature was required to break the first C−H bond

https://doi.org/10.1021/acsomega.1c06348
ACS Omega 2022, 7, 8536−8546

in methane on the surface of NiO-500. The bands located at 1390, 1592, and 1726 cm^{-1} corresponded to the $\nu_s(COO^-)$, $\nu_{as}(COO^-)$, and the vibration of the C═O bonds in formic acid, respectively. The intensities gradually increased with increasing temperature, but when the temperature increased above 300 °C, there was no obvious weakening of these bands, which proves that the desorption of intermediate products on the surface of NiO-500 was more difficult, further affecting its methane catalytic activity. In general, the higher temperature required for the dissociation of methane and the more difficult desorption of intermediate products should be the main reasons for the poor catalytic activity of NiO-500. Combined with the characterization results of XPS, it can be speculated that the hydroxyl groups also play an important role in the dissociation process of methane.

4. CONCLUSIONS

$Ni(OH)_2$-200 were prepared by a very simple manual grinding method and presented a typical nanosheet structure, which can completely catalyze methane at 400 °C. The crystal structure of the sample changed from $Ni(OH)_2$ to NiO at 300 °C. The nanosheet structure began to partially agglomerate into nanoparticles at 400 °C and almost transformed into nanoparticles at 500 °C. Interestingly, $Ni(OH)_2$-200 and NiO-300 still maintained their morphology and structure although they all went through the activity test at 500 °C in a 1.0% CH_4 atmosphere, which proves that the calcination of NiO nanosheets in a CH_4 atmosphere tended to maintain their nanosheet morphology compared to calcination in the air. It is proved that the more adsorbed oxygen and hydroxyl groups on the surface of $Ni(OH)_2$-200 were beneficial to the dissociation of methane on the catalyst, and the activation energy of methane was lowered. The methane catalytic mechanism on the surface of $Ni(OH)_2$ nanosheets and NiO nanoparticles was proposed, which further proved the key role of hydroxyl groups in methane combustion.

■ ASSOCIATED CONTENT

Supporting Information

The Supporting Information is available free of charge at https://pubs.acs.org/doi/10.1021/acsomega.1c06348.

Characterization and activity test parameters, stability test results, methane combustion activity results on other reported catalysts, and frequencies of functional groups (PDF)

■ AUTHOR INFORMATION

Corresponding Author

Wenzhi Li − *Laboratory of Basic Research in Biomass Conversion and Utilization, University of Science and Technology of China, Hefei 230026, PR China; Institute of Energy, Hefei Comprehensive National Science Center, Hefei 230031, PR China;* orcid.org/0000-0002-7082-5839; Phone: +86 0551 63600786; Email: liwenzhi@ustc.edu.cn, liwenzhi311@163.com; Fax: +86 0551 63600786

Authors

Kun Chen − *Laboratory of Basic Research in Biomass Conversion and Utilization, University of Science and Technology of China, Hefei 230026, PR China*

Ge Guo − *Laboratory of Basic Research in Biomass Conversion and Utilization, University of Science and Technology of China, Hefei 230026, PR China*

Chen Zhu − *Laboratory of Basic Research in Biomass Conversion and Utilization, University of Science and Technology of China, Hefei 230026, PR China*

Wenjian Wu − *Laboratory of Basic Research in Biomass Conversion and Utilization, University of Science and Technology of China, Hefei 230026, PR China*

Liang Yuan − *National & Local Joint Engineering Research Center of Precision Coal Mining, Anhui University of Science and Technology, Huainan 232001, China*

Complete contact information is available at: https://pubs.acs.org/10.1021/acsomega.1c06348

Author Contributions

K.C.: conceptualization, investigation, preparation of materials, writing—original draft, and methodology. W.L.: writing—review and editing and funding acquisition. G.G.: writing—review and editing. C.Z.: writing—review and editing. W.W.: writing—review and editing. L.Y.: funding acquisition.

Notes

The authors declare no competing financial interest.

■ ACKNOWLEDGMENTS

This work was supported by the Major Science and Technology Projects of Anhui Province (202003a05020022) and the Key Research and Development Projects in Anhui Province (202004a06020053).

■ REFERENCES

(1) Zasada, F.; Janas, J.; Piskorz, W.; Gorczyńska, M.; Sojka, Z. Total Oxidation of Lean Methane over Cobalt Spinel Nanocubes Controlled by the Self-Adjusted Redox State of the Catalyst: Experimental and Theoretical Account for Interplay between the Langmuir−Hinshelwood and Mars−Van Krevelen Mechanisms. *ACS Catal.* **2017**, *7*, 2853−2867.

(2) Sharma, R.; Poelman, H.; Marin, G. B.; Galvita, V. V. Approaches for Selective Oxidation of Methane to Methanol. *Catalysts* **2020**, *10*, 194.

(3) Lee, J.; Kim, M. Y.; Jeon, J. H.; Lee, D. H.; Rao, K. N.; Oh, D. G.; Jang, E. J.; Kim, E.; Na, S. C.; Han, H. S.; Kwak, J. H. Effect of Pt pre-sintering on the durability of $PtPd/Al_2O_3$ catalysts for CH_4 oxidation. *Appl. Catal., B* **2020**, *260*, 118098.

(4) Wang, C.; Wang, Y.; Chen, M.; Liang, D.; Yang, Z.; Cheng, W.; Tang, Z.; Wang, J.; Zhang, H. Recent advances during CH_4 dry reforming for syngas production: A mini review. *Int. J. Hydrogen Energy* **2021**, *46*, 5852−5874.

(5) Agarwal, N.; Freakley, S. J.; McVicker, R. U.; Althahban, S. M.; Dimitratos, N.; He, Q.; Morgan, D. J.; Jenkins, R. L.; Willock, D. J.; Taylor, S. H.; Kiely, C. J.; Hutchings, G. J. Aqueous Au-Pd colloids catalyze selective CH_4 oxidation to CH_3OH with O_2 under mild conditions. *Science* **2017**, *358*, 223−227.

(6) Li, C.; Li, W.; Chen, K.; Ogunbiyi, A. T.; Zhou, Z.; Duan, Q.; Xue, F. Highly active Pd catalysts supported on surface-modified cobalt-nickel mixed oxides for low temperature oxidation of lean methane. *Fuel* **2020**, *279*, 118372.

(7) Duan, Q.; Zhang, C.; Sun, S.; Pan, Y.; Zhou, X.; Liu, Y.; Chen, K.; Li, C.; Wang, X.; Li, W. Atomically dispersed palladium-based catalysts obtained via constructing a spatial structure with high performance for lean methane combustion. *J. Mater. Chem. A* **2020**, *8*, 7395−7404.

(8) Boukha, Z.; Choya, A.; Cortes-Reyes, M.; de Rivas, B.; Alemany, L. J.; Gonzalez-Velasco, J. R.; Gutierrez-Ortiz, J. I.; Lopez-Fonseca, R. Influence of the calcination temperature on the activity of

hydroxyapatite-supported palladium catalyst in the methane oxidation reaction. *Appl. Catal., B* **2020**, *277*, 119280.
(9) Ercolino, G.; Stelmachowski, P.; Grzybek, G.; Kotarba, A.; Specchia, S. Optimization of Pd catalysts supported on Co_3O_4 for low-temperature lean combustion of residual methane. *Appl. Catal., B* **2017**, *206*, 712−725.
(10) Zou, X.; Ma, Z. L.; Deng, J. L.; Zhong, J. J.; He, Y. B.; Liu, J. Core-shell PdO@SiO_2/Al_2O_3 with sinter-resistance and water-tolerance promoting catalytic methane combustion. *Chem. Eng. J.* **2020**, *396*, 125275.
(11) Zhang, Y.; Zhu, J.; Li, S.; Xiao, Y.; Zhan, Y.; Wang, X.; Au, C.-t.; Jiang, L. Rational design of highly H_2O- and CO_2-tolerant hydroxyapatite-supported Pd catalyst for low-temperature methane combustion. *Chem. Eng. J.* **2020**, *396*, 125225.
(12) Ding, Y.; Wu, Q.; Lin, B.; Guo, Y.; Guo, Y.; Wang, Y.; Wang, L.; Zhan, W. Superior catalytic activity of a Pd catalyst in methane combustion by fine-tuning the phase of ceria-zirconia support. *Appl. Catal., B* **2020**, *266*, 118631.
(13) Feng, X. B.; Qu, Z. G.; Gao, H. B. Premixed lean methane/air combustion in a catalytic porous foam burner supported with perovskite $LaMn_{0.4}Co_{0.6}O_3$ catalyst with different support materials and pore densities. *Fuel Process. Technol.* **2016**, *150*, 117−125.
(14) He, L.; Fan, Y.; Bellettre, J.; Yue, J.; Luo, L. A review on catalytic methane combustion at low temperatures: Catalysts, mechanisms, reaction conditions and reactor designs. *Renew. Sustain. Energy Rev.* **2020**, *119*, 109589.
(15) Yang, J.; Peng, M.; Ren, G.; Qi, H.; Zhou, X.; Xu, J.; Deng, F.; Chen, Z.; Zhang, J.; Liu, K.; Pan, X.; Liu, W.; Su, Y.; Li, W.; Qiao, B.; Ma, D.; Zhang, T. A Hydrothermally Stable Irreducible Oxide-Modified Pd/$MgAl_2O_4$ Catalyst for Methane Combustion. *Angew. Chem., Int. Ed. Engl.* **2020**, *59*, 18522−18526.
(16) Liu, Y.; Wang, S.; Gao, D.; Sun, T.; Zhang, C.; Wang, S. Influence of metal oxides on the performance of Pd/Al_2O_3 catalysts for methane combustion under lean-fuel conditions. *Fuel Process. Technol.* **2013**, *111*, 55−61.
(17) Khan, H. A.; Hao, J.; Farooq, A. Catalytic performance of Pd catalyst supported on Zr:Ce modified mesoporous silica for methane oxidation. *Chem. Eng. J.* **2020**, *397*, 125489.
(18) Murata, K.; Ohyama, J.; Yamamoto, Y.; Arai, S.; Satsuma, A. Methane Combustion over Pd/Al_2O_3 Catalysts in the Presence of Water: Effects of Pd Particle Size and Alumina Crystalline Phase. *ACS Catal.* **2020**, *10*, 8149−8156.
(19) Lei, Y.; Li, W.; Liu, Q.; Lin, Q.; Zheng, X.; Huang, Q.; Guan, S.; Wang, X.; Wang, C.; Li, F. Typical crystal face effects of different morphology ceria on the activity of Pd/CeO_2 catalysts for lean methane combustion. *Fuel* **2018**, *233*, 10−20.
(20) Li, C.; Li, W.; Chen, K.; Ogunbiyi, A. T.; Zhou, Z.; Xue, F.; Yuan, L. Palladium Nanoparticles Supported on Surface-Modified Metal Oxides for Catalytic Oxidation of Lean Methane. *ACS Appl. Nano Mater.* **2020**, *3*, 12130−12138.
(21) Li, K.; Xu, D.; Liu, K.; Ni, H.; Shen, F.; Chen, T.; Guan, B.; Zhan, R.; Huang, Z.; Lin, H. Catalytic Combustion of Lean Methane Assisted by an Electric Field over Mn_xCo_y Catalysts at Low Temperature. *J. Phys. Chem. C* **2019**, *123*, 10377−10388.
(22) Wang, W. Y.; Zhou, W.; Li, W.; Xiong, X. W.; Wang, Y. H.; Cheng, K.; Kang, J. C.; Zhang, Q. H.; Wang, Y. In-situ confinement of ultrasmall palladium nanoparticles in silicalite-1 for methane combustion with excellent activity and hydrothermal stability. *Appl. Catal., B* **2020**, *276*, 119142.
(23) Yu, Q.; Liu, C. x.; Li, X. Y.; Wang, C.; Wang, X. X.; Cao, H. J.; Zhao, M. C.; Wu, G. L.; Su, W. G.; Ma, T. T.; Zhang, J.; Bao, H. L.; Wang, J. Q.; Ding, B.; He, M. X.; Yamauchi, Y.; Zhao, X. S. N-doping activated defective Co_3O_4 as an efficient catalyst for low-temperature methane oxidation. *Appl. Catal., B* **2020**, *269*, 118757.
(24) Hu, L.; Peng, Q.; Li, Y. Selective Synthesis of Co_3O_4 Nanocrystal with Different Shape and Crystal Plane Effect on Catalytic Property for Methane Combustion. *J. Am. Chem. Soc.* **2008**, *130*, 16136−16137.
(25) Zhang, W.; Díez-Ramírez, J.; Anguita, P.; Descorme, C.; Valverde, J. L.; Giroir-Fendler, A. Nanocrystalline Co_3O_4 catalysts for toluene and propane oxidation: Effect of the precipitation agent. *Appl. Catal., B* **2020**, *273*, 118894.
(26) Yang, A.-C.; Zhu, H.; Li, Y.; Cargnello, M. Support Acidity Improves Pt Activity in Propane Combustion in the Presence of Steam by Reducing Water Coverage on the Active Sites. *ACS Catal.* **2021**, *11*, 6672−6683.
(27) Wang, Z.; Huang, Z.; Brosnahan, J. T.; Zhang, S.; Guo, Y.; Guo, Y.; Wang, L.; Wang, Y.; Zhan, W. Ru/CeO_2 Catalyst with Optimized CeO_2 Support Morphology and Surface Facets for Propane Combustion. *Environ. Sci. Technol.* **2019**, *53*, 5349−5358.
(28) Jian, Y.; Tian, M.; He, C.; Xiong, J.; Jiang, Z.; Jin, H.; Zheng, L.; Albilali, R.; Shi, J.-W. Efficient propane low-temperature destruction by Co_3O_4 crystal facets engineering: Unveiling the decisive role of lattice and oxygen defects and surface acid-base pairs. *Appl. Catal., B* **2021**, *283*, 119657.
(29) Mkhwanazi, T.; Farahani, M. D.; Mahomed, A. S.; Singh, S.; Friedrich, H. B. Engineering of catalytic sites of $Pd_xCe_{1-x}O_{2-\delta}$ for dehydrogenation, oxygen insertion and reverse water gas shift reactions during methane combustion. *Appl. Catal., B* **2020**, *275*, 119118.
(30) Chen, J.; Wang, X.; Zhang, L.; Rui, Z. Strong metal-support interaction assisted redispersion strategy for obtaining ultrafine and stable IrO_2/Ir active sites with exceptional methane oxidation activity. *Appl. Catal., B* **2021**, *297*, 120410.
(31) He, L.; Fan, Y.; Luo, L.; Bellettre, J.; Yue, J. Preparation of Pt/γ-Al_2O_3 catalyst coating in microreactors for catalytic methane combustion. *Chem. Eng. J.* **2020**, *380*, 122424.
(32) Zhang, Y.; Glarborg, P.; Andersson, M. P.; Johansen, K.; Torp, T. K.; Jensen, A. D.; Christensen, J. M. Sulfur poisoning and regeneration of Rh-ZSM-5 catalysts for total oxidation of methane. *Appl. Catal., B* **2020**, *277*, 119176.
(33) Wang, Y.; Liu, C.; Liao, X.; Liu, Y.; Hou, J.; Pham-Huu, C. Enhancing oxygen activation on high surface area Pd-SnO_2 solid solution with isolated metal site catalysts for catalytic CH_4 combustion. *Appl. Surf. Sci.* **2021**, *564*, 150368.
(34) Murata, K.; Shiotani, T.; Ohyama, J.; Wakabayashi, R.; Maruoka, H.; Kimura, T.; Satsuma, A. Relationship between penta-coordinated Al^{3+} sites in the Al_2O_3 supports and CH_4 combustion activity of Pd/Al_2O_3 catalysts. *Catal. Sci. Technol.* **2021**, *11*, 2374−2378.
(35) Chin, Y.-H.; Buda, C.; Neurock, M.; Iglesia, E. Consequences of metal-oxide interconversion for C-H bond activation during CH_4 reactions on Pd catalysts. *J. Am. Chem. Soc.* **2013**, *135*, 15425−15442.
(36) Huang, W.; Zhang, X.; Yang, A.-C.; Goodman, E. D.; Kao, K.-C.; Cargnello, M. Enhanced Catalytic Activity for Methane Combustion through in Situ Water Sorption. *ACS Catal.* **2020**, *10*, 8157−8167.
(37) Bai, S.; Yao, Q.; Xu, Y.; Cao, K. L.; Huang, X. Q. Strong synergy in a lichen-like RuCu nanosheet boosts the direct methane oxidation to methanol. *Nano Energy* **2020**, *71*, 104566.
(38) Ikeda, K.; Mahyuddin, M. H.; Shiota, Y.; Yoshizawa, K. Active Catalyst for Methane Hydroxylation by an Iridium-Oxo Complex. *ACS Catal.* **2020**, *10*, 8254−8262.
(39) Petrov, A. W.; Ferri, D.; Krumeich, F.; Nachtegaal, M.; van Bokhoven, J. A.; Kröcher, O. Stable complete methane oxidation over palladium based zeolite catalysts. *Nat. Commun.* **2018**, *9*, 2545.
(40) Yang, X.; Li, Q.; Lu, E.; Wang, Z.; Gong, X.; Yu, Z.; Guo, Y.; Wang, L.; Guo, Y.; Zhan, W.; Zhang, J.; Dai, S. Taming the stability of Pd active phases through a compartmentalizing strategy toward nanostructured catalyst supports. *Nat. Commun.* **2019**, *10*, 1611.
(41) Li, D.; Xu, R.; Tian, M.; Jia, Y.; Gu, Z.; Zhu, X.; Li, K. Encapsulated Co_3O_4/(SiAl@Al_2O_3) thermal storage functional catalysts for catalytic combustion of lean methane. *Appl. Therm. Eng.* **2020**, *181*, 116012.
(42) Chen, Z.; Wang, S.; Liu, W.; Gao, X.; Gao, D.; Wang, M.; Wang, S. Morphology-dependent performance of Co_3O_4 via facile and

https://doi.org/10.1021/acsomega.1c06348
ACS Omega 2022, 7, 8536−8546

controllable synthesis for methane combustion. *Appl. Catal., A* **2016**, *525*, 94−102.
(43) Hu, W.; Shao, Z.-J.; Cao, X.-M.; Hu, P. Multi sites vs single site for catalytic combustion of methane over Co_3O_4(110): A first-principles kinetic Monte Carlo study. *Chin. J. Catal.* **2020**, *41*, 1369−1377.
(44) Ordóñez, S.; Paredes, J. R.; Díez, F. V. Sulphur poisoning of transition metal oxides used as catalysts for methane combustion. *Appl. Catal., A* **2008**, *341*, 174−180.
(45) Chen, J.; Arandiyan, H.; Gao, X.; Li, J. Recent Advances in Catalysts for Methane Combustion. *Catal. Surv. Asia* **2015**, *19*, 140−171.
(46) Li, Y.; Guo, Y.; Xue, B. Catalytic combustion of methane over M (Ni, Co, Cu) supported on ceria−magnesia. *Fuel Process. Technol.* **2009**, *90*, 652−656.
(47) García-Vázquez, M.; Satir, D.; González-Carballo, J. M.; Landon, P.; Tooze, R.; Tan, J.; Zhang, G.; García-García, F. R. The role of sulfur sinks and micro-structured supports on the performance of sulfur-sensitive non-PGM catalysts. *Appl. Catal., A* **2021**, *622*, 118201.
(48) Mo, S.; Zhang, Q.; Li, J. Q.; Sun, Y. H.; Ren, Q. M.; Zou, S. B.; Zhang, Q.; Lu, J. H.; Fu, M. L.; Mo, D. Q.; Wu, J. L.; Huang, H. M.; Ye, D. Q. Highly efficient mesoporous MnO_2 catalysts for the total toluene oxidation: Oxygen-Vacancy defect engineering and involved intermediates using in situ DRIFTS. *Appl. Catal., B* **2020**, *264*, 118464.
(49) Zhao, S.; Li, T.; Lin, J.; Wu, P.; Li, Y.; Li, A.; Chen, T.; Zhao, Y.; Chen, G.; Yang, L.; Meng, Y.; Jin, X.; Qiu, Y.; Ye, D. Engineering Co^{3+}-rich crystal planes on Co_3O_4 hexagonal nanosheets for CO and hydrocarbons oxidation with enhanced catalytic activity and water resistance. *Chem. Eng. J.* **2021**, *420*, 130448.
(50) Tang, W.; Lu, X.; Weng, J.; Gao, P.-X. NiO nanosheet array integrated monoliths for low temperature catalytic propane oxidation: A study on the promotion effect of Ce doping. *Catal. Today* **2021**, *360*, 194−203.
(51) Zheng, Y.; Li, Y.; Huang, R.; Huang, Y.; Yao, J.; Huang, B.; Dubale, A. A. Fabrication of 2D NiO Porous Nanosheets with Superior Lithium Storage Performance via a Facile Thermal-Decomposition Method. *ACS Appl. Energy Mater.* **2019**, *2*, 8262−8273.
(52) Munkaila, S.; Bentley, J.; Schimmel, K.; Ahamad, T.; Alshehri, S. M.; Bastakoti, B. P. Polymer directed synthesis of NiO nanoflowers to remove pollutant from wastewater. *J. Mol. Liq.* **2021**, *324*, 114676.
(53) Fan, Y.; Ma, Z.; Wang, L.; Dong, Y.; Jiang, T.; Li, Z.; Liu, L.; Shao, G. In-situ synthesis of NiO foamed sheets on Ni foam as efficient cathode of battery-type supercapacitor. *Electrochim. Acta* **2018**, *269*, 62−69.
(54) Hewavitharana, I. K.; Ding, Y.; Simon Ng, K. Y.; Deng, D. 1-D NiO nanorods pillared 2-D MnO_2 nanosheets as lithium-free cathode materials for charged-state lithium batteries. *Chem. Eng. Sci.* **2021**, *236*, 116480.
(55) Gou, Y.; Liang, X.; Chen, B. Catalytic hydrogenation of acetophenone over shape controlled Pd catalysts supported on sheet-like NiO. *Catal. Today* **2013**, *216*, 200−204.
(56) Liu, J.; Zhu, Y.; Wang, C.; Singh, T.; Wang, N.; Liu, Q.; Cui, Z.; Ma, L. Facile synthesis of controllable graphene-co-shelled reusable Ni/NiO nanoparticles and their application in the synthesis of amines under mild conditions. *Green Chem.* **2020**, *22*, 7387−7397.
(57) Yousaf, Z.; Sajjad, S.; Ahmed Khan Leghari, S.; Mehboob, M.; Kanwal, A.; Uzair, B. Interfacial charge transfer via 2D-NiO and 2D-graphene nanosheets combination for significant visible photo-catalysis. *J. Solid State Chem.* **2020**, *291*, 121606.
(58) Liu, J.; Wang, H.; Ye, R.; Jian, P.; Wang, L. Promotional effect of Mn-doping on the catalytic performance of NiO sheets for the selective oxidation of styrene. *J. Colloid Interface Sci.* **2021**, *585*, 61−71.
(59) Chen, C.; Wen, H.; Tang, P.-P.; Wang, P. Supported Ni@Ni_2P Core−Shell Nanotube Arrays on Ni Foam for Hydrazine Electro-oxidation. *ACS Sustainable Chem. Eng.* **2021**, *9*, 4564−4570.
(60) Ma, G.; Zhang, X.; Zhou, G.; Wang, X. Hydrogen production from methanol reforming electrolysis at NiO nanosheets supported Pt nanoparticles. *Chem. Eng. J.* **2021**, *411*, 128292.
(61) Zhou, L.-L.; Liu, P.; Ding, Y.; Xi, J.; Liu, L.; Wang, W.-K.; Xu, J. Hierarchically porous structure of two-dimensional nano-flakes assembled flower-like NiO promotes the formation of surface-activated complex during persulfate activation. *Chem. Eng. J.* **2022**, *430*, 133134.
(62) Zhang, H.; Lv, Y.; Chen, C.; Lv, C.; Wu, X.; Guo, J.; Jia, D. Inter-doped ruthenium−nickel oxide heterostructure nanosheets with dual active centers for electrochemical-/solar-driven overall water splitting. *Appl. Catal., B* **2021**, *298*, 120611.
(63) Matsuda, J.; Yamamoto, T.; Takahashi, S.; Nakanishi, H.; Sasaki, K.; Matsumura, S. In Situ TEM Investigation of Structural Changes in Ni Nanoparticle Catalysts under Gas Atmospheres: Implications for Catalyst Degradation. *ACS Appl. Nano Mater.* **2021**, *4*, 2175−2182.
(64) Deng, X. Preparation of nano-NiO by ammonia precipitation and reaction in solution and competitive balance. *Mater. Lett.* **2004**, *58*, 276−280.
(65) Li, T.; Lu, T.; Li, Y.; Yin, J.; Tang, Y.; Zhang, M.; Pang, H.; Xu, L.; Yang, J.; Zhang, Y. Interfacial engineering-induced electronic regulation drastically enhances the electrocatalytic oxygen evolution: Immobilization of Janus-structured NiS/NiO nanoparticles onto carbon nanotubes/nanofiber-integrated superstructures. *Chem. Eng. J.* **2022**, *428*, 131094.
(66) Li, Q.; Zheng, S.; Du, M.; Pang, H. Ultrathin nanosheet metal−organic framework@NiO/Ni nanorod composites. *Chem. Eng. J.* **2021**, *417*, 129201.
(67) Ren, X.; Guo, C.; Xu, L.; Li, T.; Hou, L.; Wei, Y. Facile Synthesis of Hierarchical Mesoporous Honeycomb-like NiO for Aqueous Asymmetric Supercapacitors. *ACS Appl. Mater. Interfaces* **2015**, *7*, 19930−19940.
(68) Fu, E.; Qiu, Y.; Lu, H.; Wang, S.; Liu, L.; Feng, H.; Yang, Y.; Wu, Z.; Xie, Y.; Gong, F.; Xiao, R. Enhanced NH_3 decomposition for H_2 production over bimetallic M (M=Co, Fe, Cu) Ni/Al_2O_3. *Fuel Process. Technol.* **2021**, *221*, 106945.
(69) Ye, Y.; Zhao, Y.; Ni, L.; Jiang, K.; Tong, G.; Zhao, Y.; Teng, B. Facile synthesis of unique NiO nanostructures for efficiently catalytic conversion of CH_4 at low temperature. *Appl. Surf. Sci.* **2016**, *362*, 20−27.
(70) Yu, F.; Xu, X.; Peng, H.; Yu, H.; Dai, Y.; Liu, W.; Ying, J.; Sun, Q.; Wang, X. Porous NiO nano-sheet as an active and stable catalyst for CH_4 deep oxidation. *Appl. Catal., A* **2015**, *507*, 109−118.
(71) Xu, X.; Li, L.; Yu, F.; Peng, H.; Fang, X.; Wang, X. Mesoporous high surface area NiO synthesized with soft templates: Remarkable for catalytic CH_4 deep oxidation. *Mol. Catal.* **2017**, *441*, 81−91.
(72) Chen, K.; Li, W.; Li, X.; Ogunbiyi, A. T.; Yuan, L. Irregularly Shaped NiO Nanostructures for Catalytic Lean Methane Combustion. *ACS Appl. Nano Mater.* **2021**, *4*, 5404−5412.
(73) Wang, Y.; Chen, Y.; Wang, J.; Xv, X.; Yang, X.; Zhou, J.; Li, S.; Cao, F.; Qin, G. Novel porous ultrathin NiO nanosheets for highly efficient water vapor adsorption-desorption. *Sep. Purif. Technol.* **2019**, *226*, 299−303.
(74) Chen, J.; Zhong, J.; Wu, Y.; Hu, W.; Qu, P.; Xiao, X.; Zhang, G.; Liu, X.; Jiao, Y.; Zhong, L.; Chen, Y. Particle Size Effects in Stoichiometric Methane Combustion: Structure−Activity Relationship of Pd Catalyst Supported on Gamma-Alumina. *ACS Catal.* **2020**, *10*, 10339−10349.
(75) Du, J.; Guo, M.; Zhang, A.; Zhao, H.; Zhao, D.; Wang, C.; Zheng, T.; Zhao, Y.; Luo, Y. Performance, structure and kinetics of Pd catalyst supported in Ba modified γ-Al_2O_3 for low temperature wet methane oxidation. *Chem. Eng. J.* **2022**, *430*, 133113.
(76) Guan, S.; Huang, Q.; Ma, J.; Li, W.; Ogunbiyi, A. T.; Zhou, Z.; Chen, K.; Zhang, Q. HCHO Removal by $MnO_{2(x)}$−CeO_2: Influence of the Synergistic Effect on the Catalytic Activity. *Ind. Eng. Chem. Res.* **2019**, *59*, 596−608.
(77) Tsai, W.-T.; Yang, J.; Hsu, H.; Lin, C.; Lin, K.; Chiu, C. Development and characterization of mesoporosity in eggshell ground

https://doi.org/10.1021/acsomega.1c06348
ACS Omega 2022, 7, 8536−8546

by planetary ball milling. *Microporous Mesoporous Mater.* **2008**, *111*, 379−386.
(78) Bohström, Z.; Lillerud, K. P. Preparation of chabazite with mesopores templated from a cationic polymer. *Microporous Mesoporous Mater.* **2018**, *271*, 295−300.
(79) Chen, K.; Li, W.; Zhou, Z.; Huang, Q.; Liu, Y.; Duan, Q. Hydroxyl groups attached to Co^{2+} on the surface of Co_3O_4: a promising structure for propane catalytic oxidation. *Catal. Sci. Technol.* **2020**, *10*, 2573−2582.
(80) Chen, J.; Zou, X.; Rui, Z.; Ji, H. Deactivation Mechanism, Countermeasures, and Enhanced CH_4 Oxidation Performance of Nickel/Cobalt Oxides. *Energy Technol.* **2020**, *8*, 1900641.

https://doi.org/10.1021/acsomega.1c06348
ACS Omega 2022, 7, 8536−8546